

A TEM Study of Cobalt-Base Alloy Prototypes Fabricated by EBM

Sara M. Gaytan, Larry E. Murr, Diana A. Ramirez, Brenda I. Machado, Edwin Martinez, Daniel H. Hernandez, Jose L. Martinez, Francisco Medina, Ryan B. Wicker

University of Texas at El Paso, El Paso, USA.
Email: smgaytan@miners.utep.edu

Received February 1st, 2011; revised March 15th, 2011; accepted April 1st, 2011.

ABSTRACT

A novel microstructural architecture consisting of $Cr_{23}C_6$ carbide spatial columns was created in solid components of Co-26Cr-6Mo-0.2C fabricated from powder by additive manufacturing using electron beam melting. These columns of carbides extended in the build direction and are formed by the x-y rastering of the electron beam to pre-heat and melt powder layers using CAD models. These microstructural architectures are similar to rapidly solidified/unidirectionally solidified structures created by heat extraction in the direction perpendicular to the build plane. These columnar carbide architectures were observed by optical metallography and transmission electron microscopy (TEM) and compared with intrinsic stacking fault microstructures observed in annealed components. The TEM analysis allowed the details of the carbide crystal structure and corresponding cubic morphology to be observed.

Keywords: Electron Beam Melting, Stacking Faults, Precipitates

1. Introduction

There have been significant developments in the creation and applications of metals and alloys over the past decades (since about 1960) when the discipline of materials science and engineering emerged, embodying the structure-properties-processing-performance paradigm [1,2]. Despite the discoveries and associated improvements in the properties and performance of metals and alloys, there remain limitations in structural/(microstructural) control inherent in conventional (bulk) processing and processing routes. These are consistent with the corresponding materials science and engineering paradigm limitations in the range of achievable properties and performance. While it is common to modify material microstructures to achieve predictable property variations such as hardness, strength (and elastic modulus), toughness, thermal and electrical conductivity and the like, the controlled development of spatial arrangements of microstructural features (or architectures) such as directional solidification has produced columnar arrays of fibers, especially eutectic fibers, which provide directional properties [3-5]. Similar processing routes have recently been demonstrated by additive manufacturing (AM) using electron beam melting (EBM) for the fabrication of

Co-base alloy (Co-26Cr-6Mo-0.2C) components [6], and a Ni-base superalloy where columnar Ni_3Nb precipitates were formed [7]. In this prior Co-base alloy study [6] $Cr_{23}C_6$ precipitates were observed to form spatial arrays of carbide columns generally in the EBM build direction as a consequence of unique thermodynamic zone arrays characteristic of the electron beam preheat and melt-raster geometry which was conducive to carbide precipitate formation. It has been stated by Stoloff and others that cobalt-base alloys are hardened by precipitation of either carbides or intermetallic compounds [8].

This paper examines the microstructural architecture characterized mainly by spatial columns of $Cr_{23}C_6$ carbides and dislocations which occur in solid Co-base alloy prototypes fabricated by EBM. CoCrMo has a high corrosion resistance due to the high chromium content that forms a thin passive oxide layer, which makes it an ideal candidate for metal-on-metal bearing surfaces in orthopaedic implants. This alloy also provides a high wear resistance depending on the size, shape and distribution of carbide precipitates [9]. A study conducted by Cawley *et al.*, basically consisted in comparing the microstructures of the same Co-Cr-Mo alloy as cast, wrought and with different heat treatments, finding that the carbides obtained from all the thermally processed samples were

richer in chromium than molybdenum and no difference in hardness was obtained from the as-cast and the thermally treated materials [10]. We demonstrate these architectures by constructing and comparing 3D image composites from optical microscopy and transmission electron microscopy (TEM). Intrinsic stacking faults characteristic of the Co-rich fcc, low stacking fault energy crystal structure are also observed in the background of these microstructures, and become the dominant microstructure upon appropriate annealing to cause carbide dissolution and dislocation annihilation.

2. Experimental Methods and Procedures

Although we have described the EBM-AM process in detail elsewhere [6,11], it will provide a necessary context if we outline the process briefly herein. We begin by providing an overview of the Arcam A2-EBM system as illustrated in **Figure 1**. The major components illustrated in **Figure 1** are the electron-optical column (1) which focuses and scans the electron beam (in vacuum) over the building component (3) as powder is supplied by gravity feed from the cassettes shown at (2), and raked into a layer roughly 100 μm thick. **Figure 2(a)** illustrates the Co-26Cr-6Mo-0.2C powder (with nominal size of 40 μm) used in this study while **Figure 2(b)** shows some simple component geometries fabricated.

Figure 2(a) shows Co-26Cr-6Mo-0.2C powder observed in the SEM. As implicit in **Figure 1**, the electron beam is rastered orthogonally (x - y) in multiple passes to preheat each powder layer to roughly 830°C. This is followed by a melt scan (x , y) at reduced beam current and scan rate which builds component geometries layer-by-

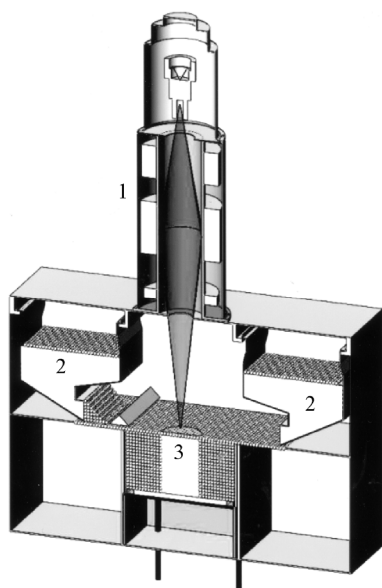


Figure 1. Arcam A2 EBM system.

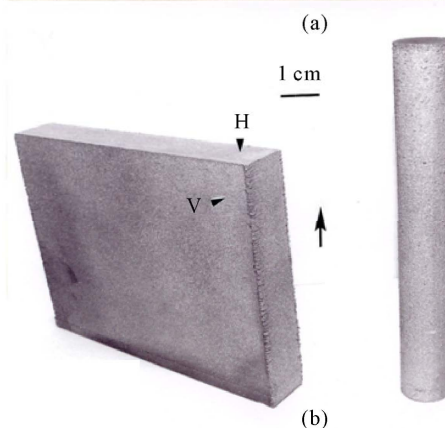


Figure 2. (a) Precursor powder; (b) Components fabricated by EBM.

layer in a direction shown by the arrow in **Figure 2(b)**. Horizontal and vertical planes (perpendicular to and parallel to the build direction) are noted by H and V, respectively in **Figure 2(b)**. The rectangular block and cylindrical components fabricated as illustrated in **Figure 2(b)** were observed to be essentially fully dense, with a density of 8.4 g/cm^3 .

Optical metallography (OM) on extracted sections from rectangular block and cylindrical builds illustrated in **Figure 2(b)** was a precursor characterization prior to developing TEM thin foils.

We employed a Reichert MEF4 A/M metallographic system for extracted specimens which were ground, polished, and etched with a 6:1 HCl: H_2O_2 (3%) etchant for 16 h at room temperature ($\sim 22^\circ\text{C}$). Annealed samples were etched in much less time (~ 2 min.). The annealing conditions involved HIP at $\sim 1200^\circ\text{C}$ for 4 h in Ar followed by a quench from a homogenizing treatment at 1220°C for 4 h in Ar at a quench rate of $\sim 7.5^\circ\text{C}/\text{min}$. As illustrated in **Figures 3 (a)** and **(b)**, OM was conducted for both the horizontal (H) and vertical (V) planes.

As illustrated in **Figure 3(c)**, specimens extracted from the EBM-fabricated components as in **Figure 3(a)** and **3(b)**

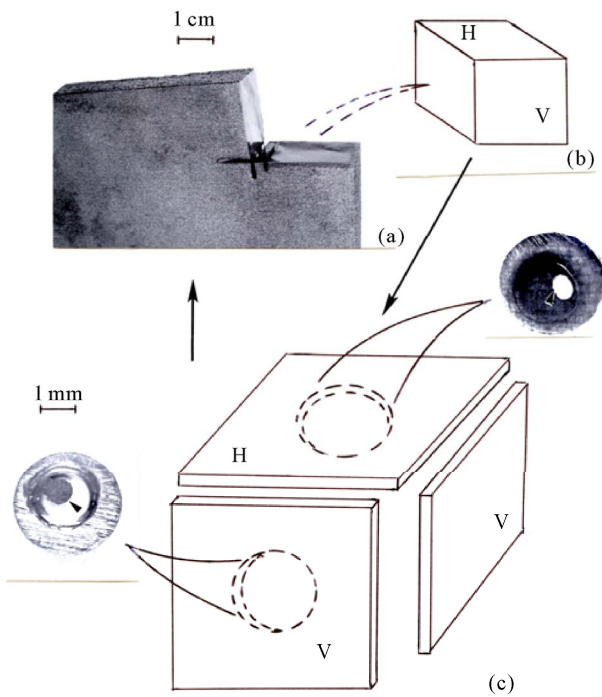


Figure 3. TEM samples obtained from block component in vertical and horizontal plane.

were also sliced using a diamond saw along the H and V planes and smaller coupons cut from these slices, ground to ~ 0.2 mm thickness, and 3 mm discs punched from these ground coupons. These discs were mechanically dimpled and electropolished in a Tenupol-5 dual jet unit at temperatures ranging from 30°C - 40°C using an electropolishing solution consisting of 15% perchloric acid and 85% acetic acid, at 20 V and 3 - 30 mA. Punched and electropolished 3 mm discs are shown in the inserts in **Figure 3(c)**.

3. Results and Discussion

3.1. Block Component Fabricated by Electron Beam Melting

Figure 4 shows an OM 3D composite for an extracted, polished, and etched specimen as illustrated in **Figures 3(a)** and **(b)** forming Cr_{23}C_6 carbide columns with spacings determined largely by the electron beam focus and scan geometry, including the spatial dimensions of the X-Y scans. **Figure 5** illustrates this processing feature in the EBM. The columns are generally parallel to the build direction marked by the arrows in **Figures 4** and **5**.

The microstructure (microstructural architecture or carbide columns in **Figure 4**) is similar to structures developed by rapid solidification or directional solidification [3-5], by heat extraction in the build direction. As the electron beam scans and melts the powder the spatial,

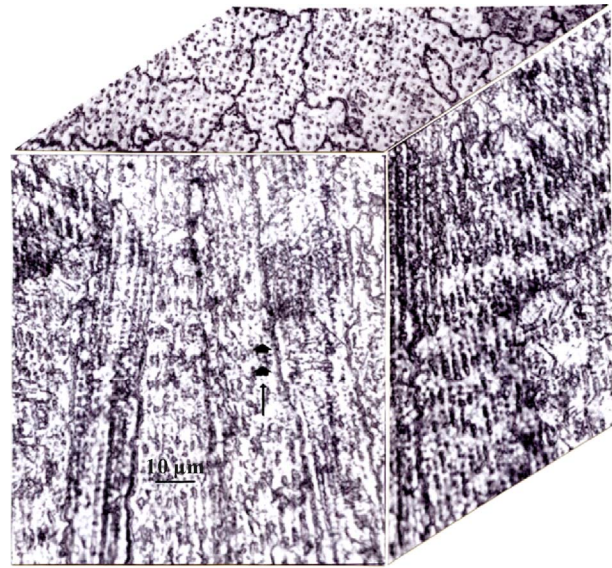


Figure 4. OM 3D composite for a block component.

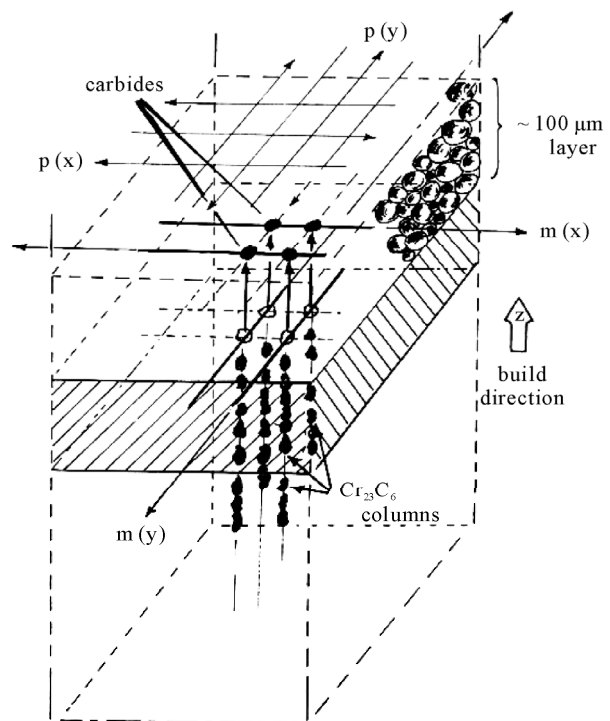


Figure 5. Carbide precipitate architecture as fabricated by EBM.

small liquid volume rapidly cools, solidifying with a plane front or cellular liquid/solid interface (**Figure 5**). The carbon within these zone segregates to the boundaries of the cellular interface, resulting in the columnar of aligned Cr_{23}C_6 precipitates. These features can be varied somewhat as described for precipitate columns formed by EBM in a Ni-base (Inconel 718) alloy [7], and in the

production of α -phase columnar grains in the selective laser melting (SLM) of Ti-6Al-4V [9]. In the SLM study [12], energy density, scanning velocity, and hatch spacing (shown schematically in **Figure 5**) were referred to as a scanning strategy which can be used to manipulate associated microstructures and microstructural architecture.

Figures 6 and **7** show 3D section views observed in the TEM at low and high magnification, respectively. The TEM views show the carbide columns in **Figure 4** to be spaced Cr_{23}C_6 , incoherent carbide precipitates. **Figure 7** in particular shows clearly the incoherent cubic (fcc: $a = 1.07 \text{ nm}$) Cr_{23}C_6 particles spaced roughly 100 to 200 nm in the EBM fabricated columns which are correspondingly spaced $\sim 2 - 3 \mu\text{m}$ as illustrated in both **Figures 4** and **6**. Contrast fringes indicating linear stacking-fault features are apparent in both the horizontal (H) and vertical (V) plane views in **Figure 7** along with dense dislocation arrangements intermingled with the carbide precipitates. These features are also observed at higher magnifications as shown in **Figure 8** which illustrates individual precipitate cubes and related crystal geometries measuring ~ 100 to 200 nm on a side.

Figures 9 to **11** show several examples of the dense intrinsic stacking-fault arrangements intercalated with dense dislocation structures. The selected-area electron diffraction (SAED) pattern insert in **Figure 9** shows micro-twin and double-diffraction spots indicative of regions of overlapping intrinsic stacking faults on every $\{111\}$ plane in the Co-rich fcc matrix ($a = 0.355 \text{ nm}$). The magnified views for dense stacking-fault arrays for stacking-faults on (111) and $(\bar{1}\bar{1}1)$ planes intersecting at 90° in the (100) surface orientation are illustrated by the SAED pattern insert in **Figure 10**. The magnified view of these intersecting stacking faults is shown in **Figure 11** where dense stacking faults intersecting at 90° for faults on $\{111\}$ planes inclined $\sim 55^\circ$ to the (100) surface plane, and in the $\langle 022 \rangle$ trace directions are shown. Similar but far less dense intrinsic stacking-fault arrays were demonstrated in the prior work of Atamert and Bhadeshia [13] for nominal compositions of Co-28Cr-4.8W-1.3C (Stellite 6). In addition, the observations in **Figures 8** to **11** illustrate stacking faults on all $\{111\}$ variant planes in contrast to observations of the favoring of a particular variant by Atamert and Bhadeshia [13]. The corresponding Rockwell C-scale hardness (HRC) values for the horizontal/vertical planes as in **Figure 4** were observed to be 44/46.

3.2. Cylindrical Component Fabricated by Electron Beam Melting

Figure 12 shows similar Cr_{23}C_6 carbide column architectures in a representative cylindrical specimen as arrays

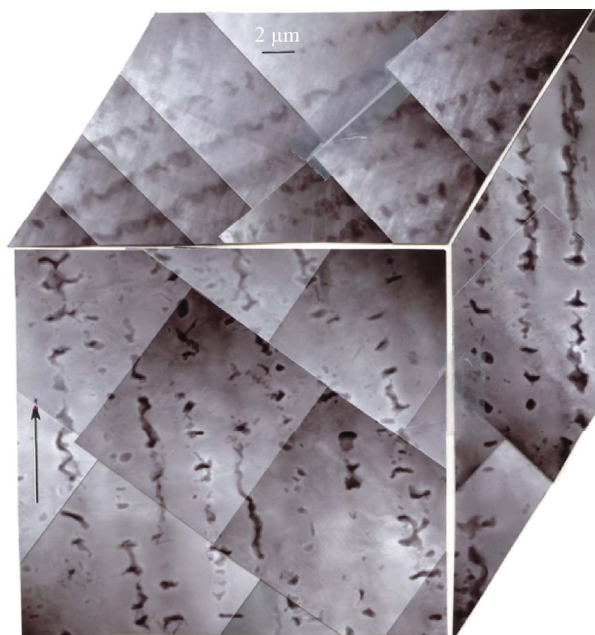


Figure 6. 3D TEM representation of carbide columns.

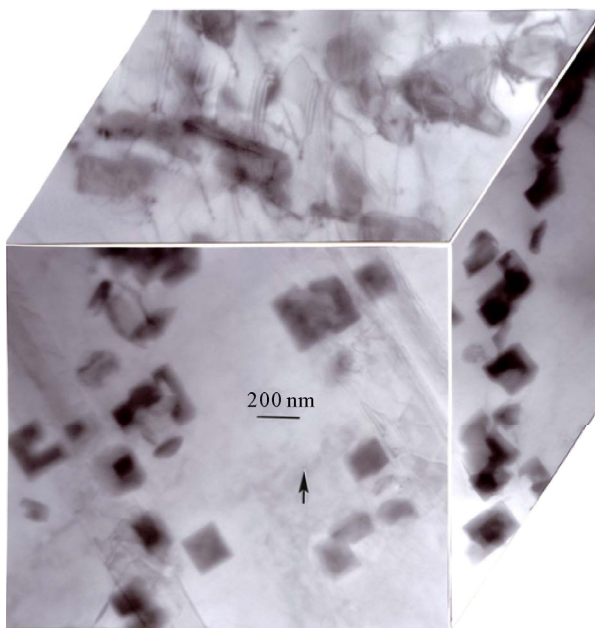


Figure 7. 3D TEM representation at higher magnification.

observed in both the horizontal and vertical planes are essentially the same as shown for the fabricated block in **Figure 4**. The associated HRC values are correspondingly 47/48. In **Figure 13**, the horizontal (OM) carbide array in **Figure 13(a)** is compared with corresponding TEM images for the same horizontal orientation. The SAED pattern insert in **Figure 13(c)** shows a (100) plane orientation with superimposed Cr_{23}C_6 carbide reflections, and these features are shown for aggregated carbide precipitates in

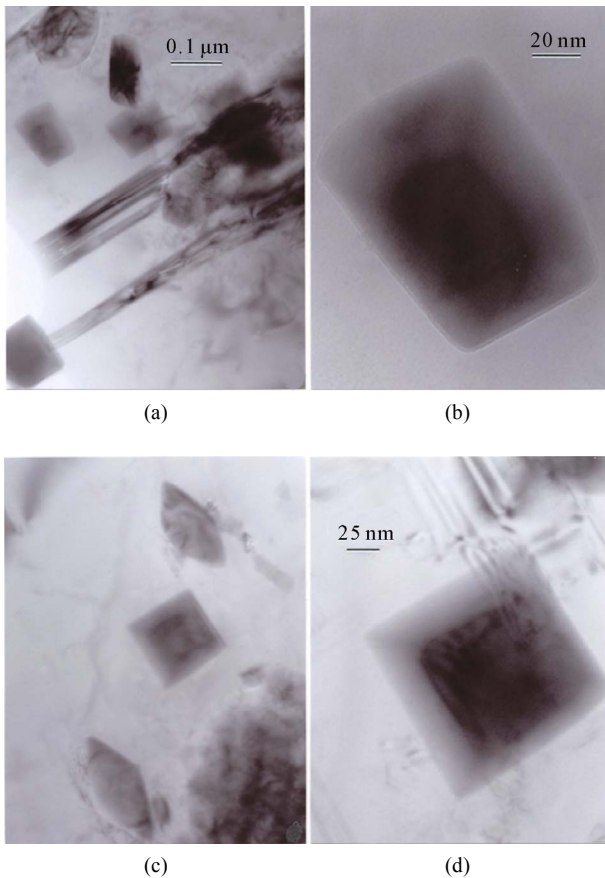


Figure 8. Cr_{23}C_6 precipitates.

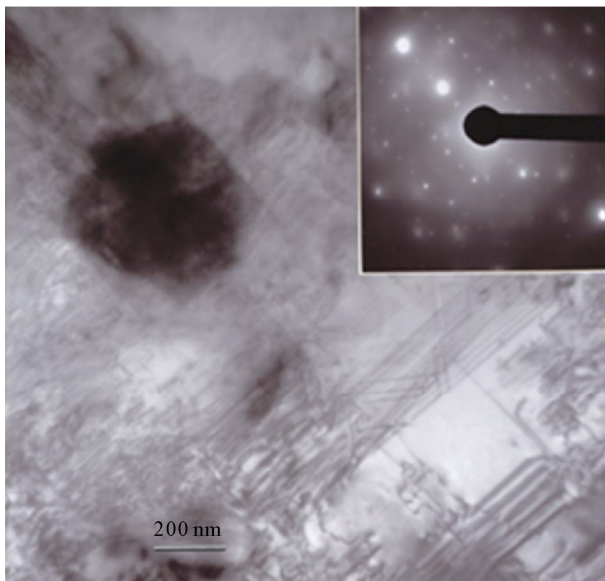


Figure 9. Stacking faults and double-diffraction spots.

Figure 14 which range in particle size from ~50 to 500 nm, with their (100)-fcc diffraction pattern superimposed on the Co-rich matrix SAED pattern insert in Figure 14.

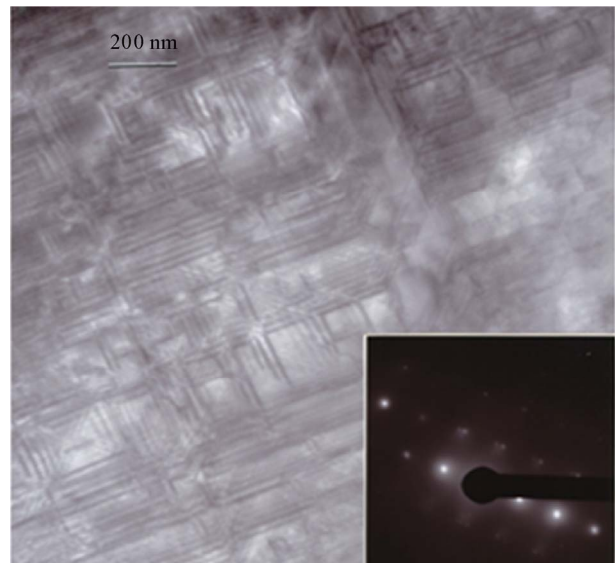


Figure 10. Intersecting intrinsic stacking faults.

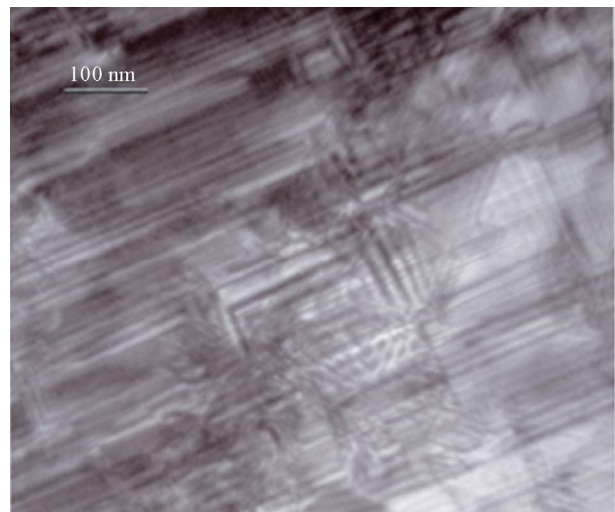


Figure 11. Magnified image of stacking faults.

Figure 14 also shows a high density of dislocations especially associated with the carbide precipitates, the SAED pattern insert shows $[100]$ Cr_{23}C_6 zone axis superimposed on $[112]$ fcc Co-rich matrix zone axis. Figure 15 shows dense stacking-fault arrays similar to those shown in Figures 9-11 for a block specimen (Figure 3). Here again, the intersections of faults on $\{111\}$ planes which intersect at 90° produce diffraction contrast features for these intersecting $\{111\}$ planes at 45° . The SAED pattern insert in Figure 15 also shows the same (100) orientation as observed in Figures 9-11, along with some extra reflections characteristic of twin faults created by the systematic, overlapping intrinsic stacking faults.

As shown previously by Gaytan, *et al.* [6], the fracture surface for failed cylindrical samples illustrated a spatial

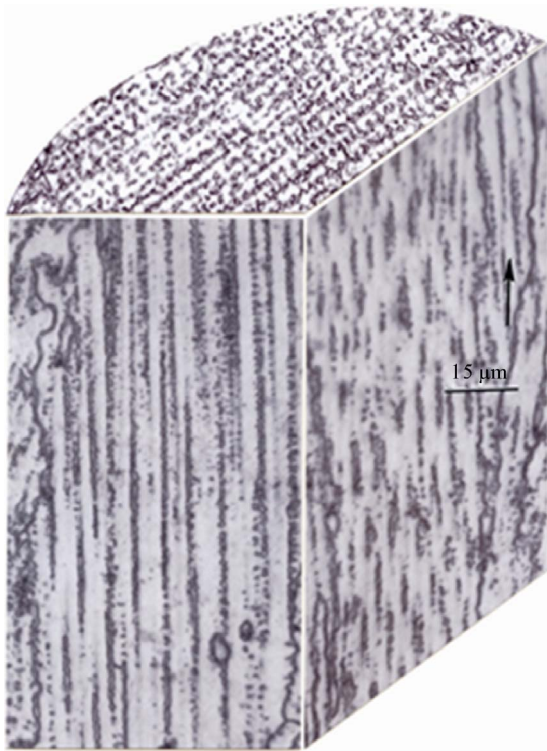


Figure 12. Columnar architecture in cylindrical component.

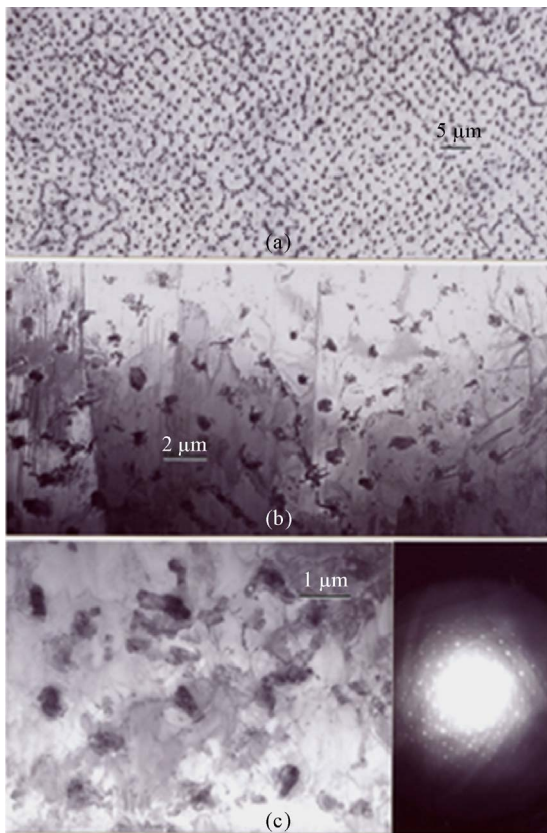


Figure 13. OM and TEM images of carbides.

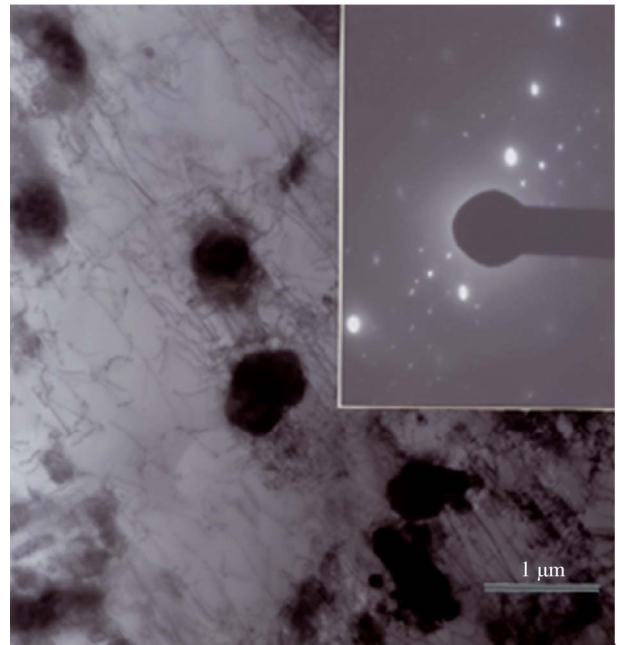


Figure 14. $Cr_{23}C_6$ particles interacting with or generating dislocations.

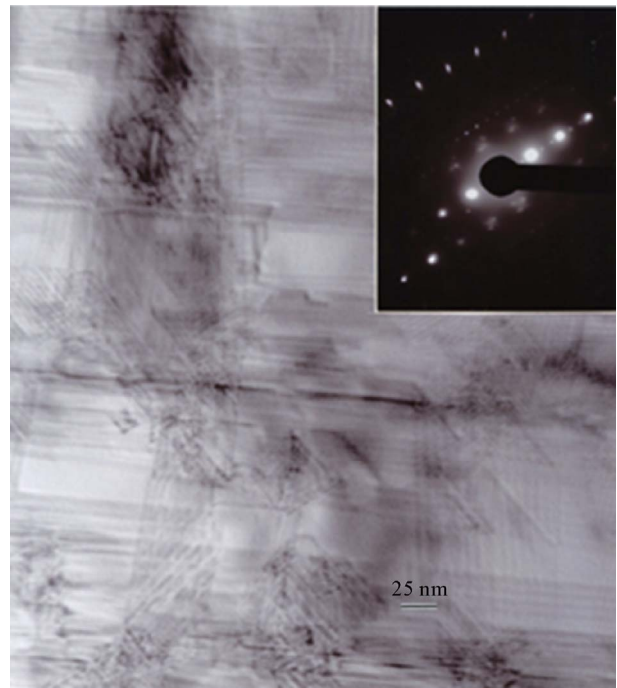


Figure 15. Dense, intersecting stacking faults.

array of ductile dimples matching the cubic-shape carbide precipitate array illustrated typically in **Figures 12** and **13** in the horizontal plane, coincident with the fracture surface; this feature is illustrated in **Figure 16**. Corresponding UTS and elongation were 1.45 GPa and 3.6%, respectively, as previously determined by Gaytan, *et al.* [6].

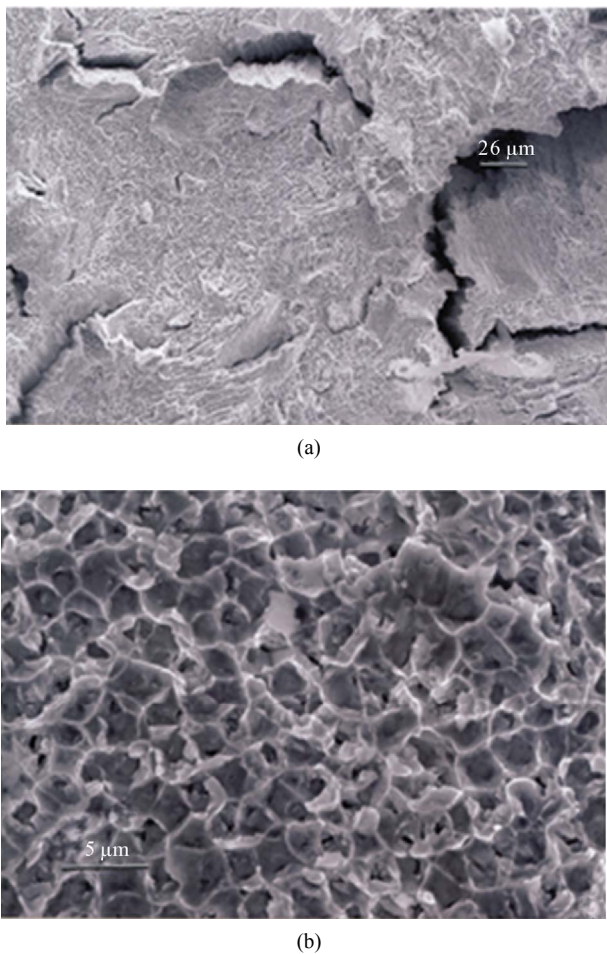


Figure 16. Fractured surface from a cylindrical component fabricated by EBM, (a) Low magnification and (b) High magnification image.

Grain boundaries and regular grain structures were difficult to differentiate in the carbide arrays but more regular Cr_{23}C_6 precipitation and corresponding etching made them somewhat apparent as noted in the etching patterns of **Figure 4**. Here the average grain sizes are observed to be about $20\ \mu\text{m}$, or an order of magnitude larger than the carbide column arrays. There seems to be a preference for $[100]$ orientations parallel to the build direction, which is also characteristic of orientation preference in commercial processed copper billets and plate.

3.3. Components Fabricated by Electron Beam Melting after Annealing

In the annealed condition, the carbide column architectures disappear, leaving an, fcc grain structure containing a propensity of annealing twin boundaries. While Cr_{23}C_6 carbides generally dissolve in the grain matrix, there are residual carbides in the grain boundaries, and these promote exaggerated etching, especially at high angle or high energy

grain boundaries. In this regard, note that there is no carbide-associated etching along the straight coherent twin boundaries where the energy is roughly the same as the stacking faults ($\sim 15\ \text{mJ}/\text{m}^2$), and about 0.03 times the grain boundary free energy [14]. These features are illustrated typically in **Figure 17** where the average grain size, including twinned grains (light grains) was $\sim 35\ \mu\text{m}$. This is roughly a 75% increase over the as-fabricated Co-26Cr-6Mo-0.2C components (**Figure 2(b)**). Correspondingly, the residual hardness (HRC) was 40 in contrast to ~ 47 for the as-fabricated components; a decrease of $\sim 15\%$. The high density of stacking faults and twin-faults declined measurably as illustrated in comparative views of stacking faults shown in **Figures 18-20**, where **Figure 18** represents a surface orientation of (112) with $[\bar{1}\bar{1}0]$ direction shown by the arrow. **Figure 19** is a magnified view of stacking faults in the (100) surface orientation with their traces in the $\langle 022 \rangle$ directions. **Figure 20**, like **Figures 18** and **19**, illustrates intrinsic stacking faults on essentially all $\{111\}$ plane variants in contrast to the prior Co-base alloy TEM observations by Atamert and Bhadeshia [13].

It is of interest to compare, retrospectively, the annealed, equiaxed grain structure (**Figure 17**) and the associated stacking fault microstructure (**Figures 18-20**) with the more dense stacking fault microstructure and unique carbide microstructural architectures created by EBM fabrication as illustrated in **Figures 9-11** and **15**, and **Figures 4, 6-8**, and **12-14**. **Figure 18** shows a TEM bright-field image of intrinsic stacking faults in the (112) orientation for the annealed Co-base alloy in **Figure 17**. The arrow indicates the trace of the $[\bar{1}\bar{1}0]$ direction, while **Figure 19** is a TEM image of stacking faults intersecting at $\sim 90^\circ$ in a (100) grain orientation and **Figure 20** shows multi-variant $\{111\}$ stacking faults in the annealed Co-base alloy. These comparisons provide a compelling example of a controlled microstructural architecture in contrast to the conventional (carbide) microstructural regime. Although the Cr_{23}C_6 column architectures are not continuous or even proximate carbide particles, the concept as it can be created through systematic, additive manufacturing using EBM, suggests a revolutionary extension of the conventional microstructure-property-processing-performance materials science an engineering paradigm. Indeed, in the same way compositions (in this case especially carbon content) or chemistries of alloy systems can influence the microstructure-property relationships in particular, the prospects for microstructural architecture manipulation and the attendant property-processing-performance variations, attest to the novelty and potential features of the concept. Increasing the carbon content in the Co-26Cr-6Mo-C alloy, especially to more contemporary levels for aerospace superalloy applications ($\geq 0.5\text{C}$) should have a controlling effect on the carbide particle

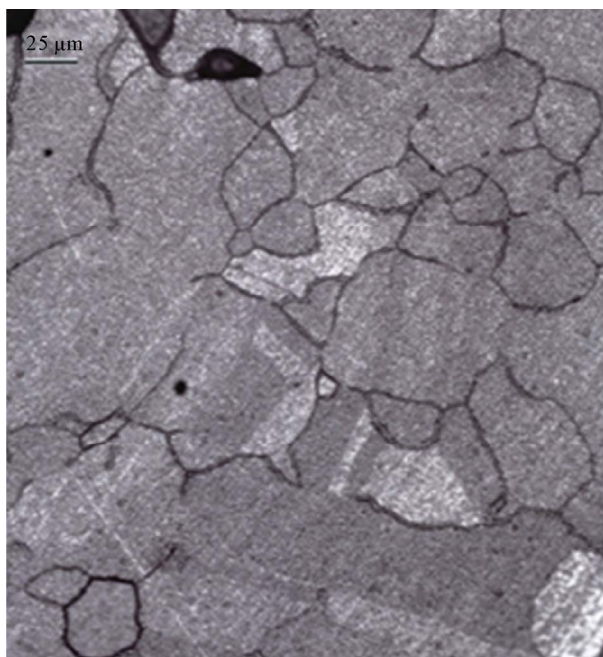


Figure 17. EBM fabricated components after annealing treatment.

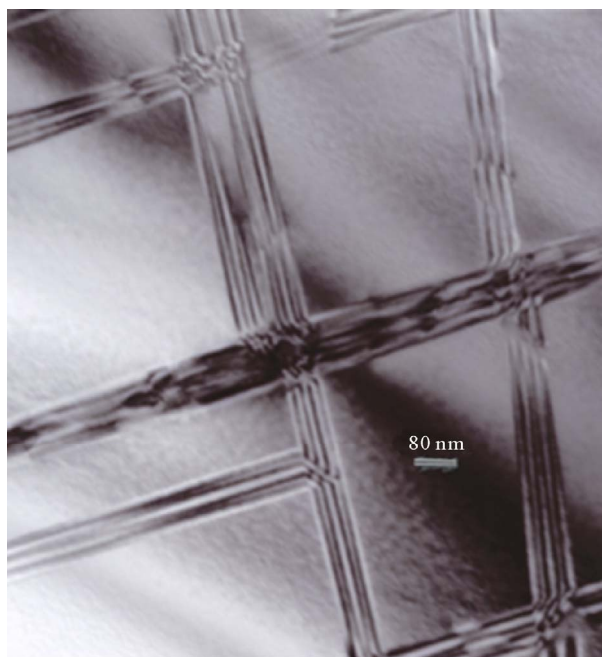


Figure 19. Stacking faults intersecting at $\sim 90^\circ$ in a (100) grain orientation.

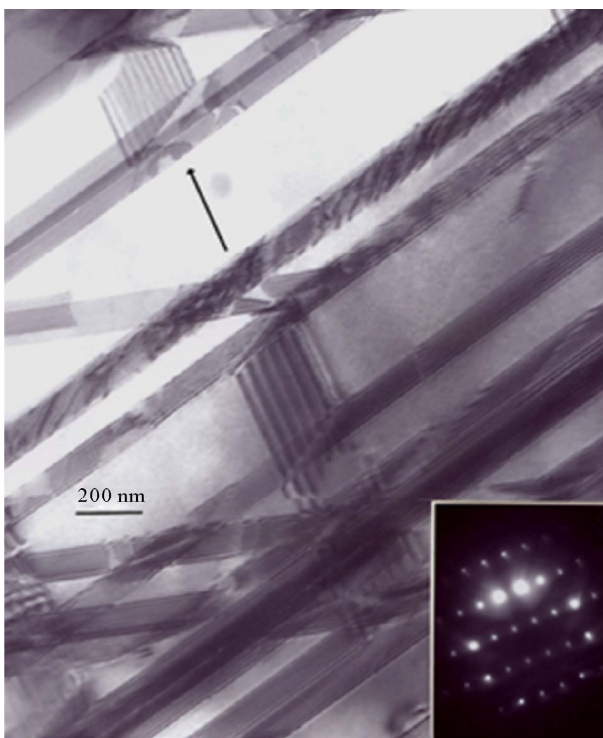


Figure 18. Intrinsic stacking faults in the (112) orientation.

densities (or spacings) in the EBM-produced columns (**Figures 4, 6 and 7**). This in turn should influence simple mechanical properties such as residual hardness (even directionally), strength, elongation, and even the elastic

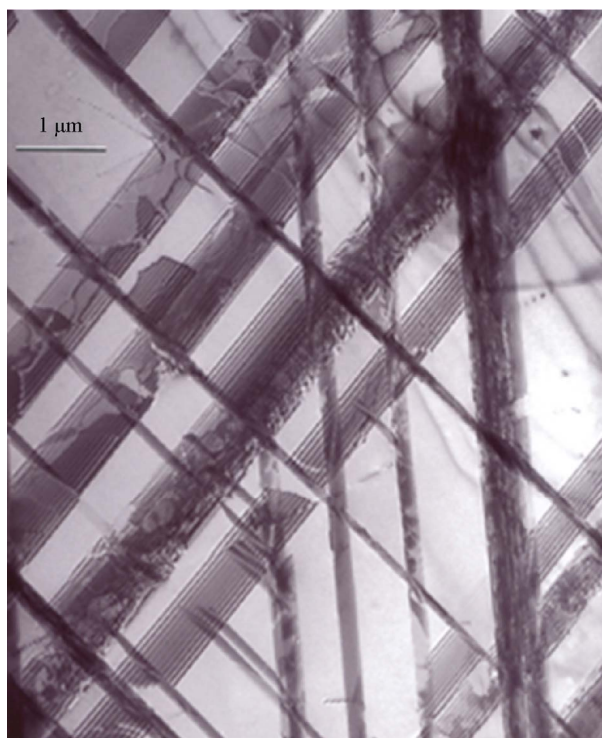


Figure 20. Multivariant {111} stacking faults in the annealed Co-base alloy.

(Young's) modulus. The latter would be especially notable if the carbide particle columns began to act somewhat like fiber-arrays in a matrix where the volumetric addition

of such reinforcing features alter the elastic modulus in relation to their spatial relationship as it influences the so-called rule of mixtures for the ideal isostrain condition where the stress is applied in the direction of the fibers. Of course these features are only speculative at this point.

4. Conclusions

Using TEM, we have illustrated the details of Cr_{23}C_6 carbide columns created by the systematic, spatial scans of an electron beam in the additive manufacturing of Co-26Cr-6Mo-0.2C prototypes using EBM. These columns represent an example of a controlled microstructural architecture. In this study, we have in principle compared these uniquely fabricated architectures with more conventional, stacking fault microstructures by annealing the carbides and their attendant architectures. These architectures represent length scales ranging from microns-to-nanometers which may be extended systematically to the macroscale represented by millimeters-to-meters. The TEM analyses have demonstrated Cr_{23}C_6 carbides to be exclusive in the formation of column architectures with spacings of 1 - 3 μm for carbide particles ranging nominally from <100 nm to >200 nm.

5. Acknowledgements

This work was supported in part by Mr. & Mrs. MacIntosh Murchison endowments at The University of Texas at El Paso.

REFERENCES

- [1] R. Roy, "Materials Science and Engineering in the United States," The Pennsylvania State University Press, State College, 1970.
- [2] Materials Science and Engineering for the 1990s, "Maintaining Competitiveness in the Age of Materials," National Academy Press, Washington, 1989.
- [3] G. A. Chadwick, "Eutectic Solidification," In: T. J. Hughel, Ed., *Liquids: Structure, Properties, Solid Interactions*, Elsevier, New York, 1965, pp. 238-255.
- [4] H. W. Weart and J. D. Mack, "Eutectic Solidification Structures," *Transactions of the Metallurgical Society of AIME*, Vol. 212, 1958, pp. 664-671.
- [5] R. W. Kraft, "Eutectic Solidification," *Journal of Metals*, Vol. 8, No. 2, 1966, pp. 192-198.
- [6] S. M. Gaytan, L. E. Murr, E. Martinez, J. L. Martinez, B. I. Machado, D. A. Ramirez, F. Medina, S. Collins and R. B. Wicker, "Comparisons of Microstructures and Mechanical Properties for Solid and Mesh Cobalt-Base Alloy Prototypes Fabricated by Electron Beam Melting," *Metallurgical and Materials Transactions A*, Vol. 41, No. 12, 2010, pp. 3216-3227. [doi:10.1007/s11661-010-0388-y](https://doi.org/10.1007/s11661-010-0388-y)
- [7] A. Strondl, R. Fischer, G. Frommeyer and A. Schneider, "Investigations of MX and γ'/γ " precipitates in the Nickel-based Superalloy 718 Produced by Electron Beam Melting," *Materials Science and Engineering A*, Vol. 480, No. 1-2, 2008, pp. 138-147. [doi:10.1016/j.msea.2007.07.012](https://doi.org/10.1016/j.msea.2007.07.012)
- [8] C. T. Sims, N. S. Stoloff and W. C. Hagel, "Superalloys II," John Wiley & Sons, New York, 1987.
- [9] G. D. Janaki, "Microstructure and Wear Properties of LENS® Deposited Medical Grade CoCrMo," *Journal of Materials Science: Materials in Medicine*, Vol. 19, No. 5, 2008, pp. 2105-2111. [doi:10.1007/s10856-007-3078-6](https://doi.org/10.1007/s10856-007-3078-6)
- [10] J. Cawley, J. E. P. Metcalf, A. H. Jones, T. J. Band and D. S. Skupien, "A Tribological Study of Cobalt Chromium Molybdenum Alloys Used in Metal-on-Metal Resurfacing Hip Arthroplasty," *Wear*, Vol. 255, No. 7-12, 2003, pp. 999-1006. [doi:10.1016/S0043-1648\(03\)00046-2](https://doi.org/10.1016/S0043-1648(03)00046-2)
- [11] L. E. Murr, E. V. Esquivel, S. A. Quinones, S. M. Gaytan, M. I. Lopez, E. Y. Martinez, F. Medina, D. H. Hernandez, E. Martinez, J. L. Martinez, S. W. Stafford, D. K. Brown, T. Hoppe, W. Meyers, U. Lindhe and R. B. Wicker, "Microstructures and Mechanical Properties of Electron Beam-Rapid Manufactured Ti-6Al-4V Biomedical Prototypes Compared to Wrought Ti-6Al-4V," *Materials Characterization*, Vol. 60, No. 2, 2009, pp. 96-105. [doi:10.1016/j.matchar.2008.07.006](https://doi.org/10.1016/j.matchar.2008.07.006)
- [12] L. Thijs, F. Verhaeghe, T. Craeghs, J. van Humbeeck and J.-P. Kruth, "A Study of the Microstructural Evolution during Selective Laser Melting of Ti-6Al-4V," *Acta Materialia*, Vol. 58, No. 9, 2010, pp. 3303-3312. [doi:10.1016/j.actamat.2010.02.004](https://doi.org/10.1016/j.actamat.2010.02.004)
- [13] S. Atamert and H. K. D. H. Bhadeshia, "Comparison of the Microstructures and Abrasive Wear Properties of Stellite Hardfacing Alloys Deposited by Arc Welding and Laser Cladding," *Metallurgical and Materials Transactions*, Vol. 20, No. 6, 1989, pp. 1037-1054. [doi:10.1007/BF02650140](https://doi.org/10.1007/BF02650140)
- [14] L. E. Murr, "Interfacial Phenomena in Metals, and Alloys," Addison-Wesley, Reading, 1975.